Research Square

Preprints are preliminary reports that have not undergone peer review.
They should not be considered conclusive, used to inform clinical practice,
or referenced by the media as validated information.

Individualized risk prediction nomogram and ultrasound signs for preoperative differentiation of struma ovarii

Wanting Chen
Chinese Academy of Medical Sciences & Peking Union Medical College
Fei Ji
Chinese Academy of Medical Sciences & Peking Union Medical College
Weihan Xiao
Chinese Academy of Medical Sciences & Peking Union Medical College
Jiajia Tang
Chinese Academy of Medical Sciences & Peking Union Medical College
Wenjing Zhao
Chinese Academy of Medical Sciences & Peking Union Medical College
Jinghui Liang
Chinese Academy of Medical Sciences & Peking Union Medical College
Na Su
sunaworld@126.com
Chinese Academy of Medical Sciences & Peking Union Medical College
Meng Yang
Chinese Academy of Medical Sciences & Peking Union Medical College

Research Article

Keywords: Struma ovarii, high-grade serous ovarian carcinoma, ultrasound signs, nomogram

Posted Date: May 13th, 2026

DOI: https://doi.org/10.21203/rs.3.rs-9459948/v1

License: This work is licensed under a Creative Commons Attribution 4.0 International License.
Read Full License

Additional Declarations: No competing interests reported.

Abstract

Objectives

Struma ovarii (SO) often presents as a multilocular-solid adnexal mass with abundant vascularity, easily misdiagnosed as an epithelial malignancy and leading to inappropriate surgical management. This study aimed to develop and validate a preoperative nomogram to differentiate O-RADS US 4/5 struma ovarii (SO) from early-stage high-grade serous carcinoma (HGSC) and to identify characteristic ultrasound signs of SO, enhancing diagnostic accuracy and clinical applicability.

Methods

This retrospective cohort study enrolled 93 SO lesions from 92 patients and 87 early-stage HGSC lesions from 79 patients at Peking Union Medical College Hospital between January 2017 and December 2025. Lesions were randomly divided into training and validation sets (7:3). Independent predictors were identified using univariate and multivariate logistic regression. An individualized risk prediction nomogram was then developed, along with a dynamic nomogram constructed using the "DynNom" and "shiny" packages in R. Model performance was evaluated using the area under the receiver operating characteristic curve, calibration curves, and decision curve analysis.

Results

Among SO cases, 65 (70.7%) were asymptomatic, 23 (25.0%) had elevated CA125 (> 35 U/mL). Ascites was present in 7 patients (7.6%). 80 lesions (86.0%) were classified as O-RADS 5, and 25 (26.9%) misdiagnosed as malignant. Most SO were pure lesions with low malignant transformation and no metastasis. 9 premenopausal patients (17.3%) underwent radical surgery, suggesting overtreatment. Multivariate logistic regression identified CA125, heterogeneous cyst fluid, comet-tail artifact, morphological pattern of the solid component, and echogenicity of the solid component as independent preoperative predictors. The clinical-ultrasound nomogram demonstrated excellent predictive performance, with an AUC of 0.971 (95% CI: 0.95–0.99) in the training set and 0.939 (95% CI: 0.88–0.99) in the validation set. Calibration curves indicated strong agreement between predicted and observed probabilities, and decision-curve analysis confirmed its clinical utility. Three typical ultrasound signs of SO—ovary-like sign, palette sign, and Cheerios sign—were summarized, and the interpretation of the “pearl sign” was refined.

Conclusion

The static and dynamic nomograms and ultrasound signs enable accurate preoperative differentiation of O-RADS US 4/5 SO from HGSC, which provide an innovative and reproducible framework for precise

preoperative decision-making.

1. Background

Struma ovarii (SO) is a rare, highly differentiated monodermal teratoma defined by thyroid tissue comprising more than 50% of the tumor [1, 2], accounting for 2–3% of teratomas and 0.5-1% of ovarian tumors [3–5]. Although malignant transformation occurs in 5–10% of cases, prognosis is generally favorable in both benign and nonmetastatic cases [6–8]. Clinical presentation is often nonspecific, asymptomatic patients may be incidentally identified during routine physical examinations or imaging screenings, which substantially increases the difficulty of preoperative diagnosis [9]. Due to its rarity, existing evidence primarily comes from case reports and small retrospective series, and standardized diagnostic and management guidelines are still lacking [10, 11].

Accurate preoperative diagnosis is crucial for appropriate management plans. Ultrasound (US) is the first-line imaging modality for adnexal masses. The Ovarian-Adnexal Reporting and Data System (O-RADS) US offers a standardized assessment framework for clinical practice [12]. However, SO often presents as a multilocular-solid mass with moderate to abundant blood flow signals on ultrasound,, classified as O-RADS 4/5 [13, 14]. magnetic resonance imaging (MRI) may show lobulated cystic-solid lesions with a "stained-glass" appearance. High signal intensity on T1-weighted images or punctate low-signal foci on T2-weighted images may also be observed [15, 16]. Additionally, high-risk time-intensity curve patterns without diffusion restriction [17, 18] lead to O-RADS MRI 5 [17, 18]. These features overestimate malignancy risk and lack reliable discriminatory value [11].

Approximately 90% of ovarian cancers are epithelial malignancies, 70% -80% of which are high-grade serous ovarian cancers (HGSC), the most common and aggressive subtype [19]. Early-stage (FIGO I-II) HGSC often appears as O-RADS US 4/-5 complex cystic-solid mass with abundant blood flow. Thus, HGSC was chosen as the primary comparator for SO due to its high incidence, making their differentiation clinically critical. More importantly, preoperative differentiation directly guides surgical strategy and patient benefit. Early-stage HGSC requires standardized staging surgery and systemic treatment [19, 20], whereas SO can generally be managed conservatively [21, 22].

Currently, no imaging-based prediction model specifically exists to preoperatively differentiate SO from early-stage ovarian cancer, and O-RADS US is insufficient. To fill this gap, we retrospectively analyzed O-RADS 4/5 SO lesions and FIGO stage I-II HGSC to develop and validate an individualized preoperative risk prediction nomogram and an interactive dynamic nomogram. We also propose three characteristic ultrasound signs for SO, which may serve as valuable imaging clues for differentiating SO from malignant ovarian cancers. This study has the potential to enhance the accuracy of preoperative risk stratification and provide a more reliable basis for surgical planning and clinical decision-making.

2. Methods

2.1 Patients

This retrospective study included patients with gynecologic surgery for ovarian masses at Peking Union Medical College Hospital between January 2017 and December 2025. Inclusion criteria were: (1) complete preoperative clinical data and evaluable ultrasound images; (2) O-RADS US 4/5 cystic-solid lesions pathologically confirmed as SO or FIGO stage I-II HGSC postoperatively. Exclusion criteria were: (1) preoperative treatment for ovarian tumors; (2) O-RADS US 1–3 lesions; and (3) incomplete clinical data or non-evaluable ultrasound images. After screening, 93 SO lesions from 92 patients and 87 early stage HGSC lesions from 79 patients were included. This retrospective study followed the Declaration of Helsinki and received approval from the Institutional Review Board of our hospital (IRB No. I-24PJ0809).

2.2 Clinical variables

Given their availability in routine practice and predictive value, key variables were from the electronic medical record system, including: (1) age; (2) family history (yes/no), breast/ovarian/gynecologic malignancies in first/second-degree relatives; (3) symptoms (yes/no), abdominal pain, distension, irregular vaginal bleeding, or palpable abdominal mass; and (4) CA125 > 35 U/mL (yes/no). All data were collated using standardized collection templates and independently verified by two investigators. Comorbidities and surgical approach were additionally recorded.

2.3 Ultrasound Examinations and Feature

Preoperative ultrasound examinations were performed by certified radiologists using standardized equipment including GE Voluson E10 (GE Healthcare, USA), Philips EPIQ 7 (Philips Healthcare, the Netherlands), and Philips iU22, with transabdominal (2.5-5.0 MHz) and transvaginal (5.0–9.0 MHz) probes. Each lesion was assessed in multiple planes, and at least two orthogonal grayscale and color Doppler images were stored. Lesions were selected and classified as according to the O-RADS US 2022 [12]. Based on expert consensus derived from extensive clinical experience, the following ultrasound variables were analyzed: (1) laterality (unilateral/bilateral); (2) largest diameter in any plane; (3) contour (regular/irregular); (4) number of locules (1, 2–4 or ≥ 5); (5) regularity of locules (yes/no); (6) homogeneity of cyst fluid (yes/ no); (7) comet_tail artifact (yes/no); (8) morphological pattern of the solid component (intracystic solid component, extracystic solid tissue or predominantly solid component). Intracystic solid component denotes a papillary projection or nodule (height ≥ 3 mm) from the cyst wall or septation protruding into the cyst cavity. Extracystic solid tissue refers to solid components distributed along the periphery of locules, presenting as ring-like or septal-like focal thickening. Predominantly solid component refers to a lesion composed of at least 80% solid tissue, with minor cystic components. (9) echogenicity of solid component (hypoechoic, isoechoic, or hyperechoic), relative to the myometrium; (10) color score (grade 0–1, 2 or 3) (11) calcification (yes/no); and (12) free intraperitoneal fluid (yes/no). All images were independently reviewed by two radiologists with over 10 years of experience in gynecological imaging. Discrepancies were confirmed by a senior expert with more than 20 years of clinical experience. All images were de -identified and randomly anonymized before analysis.

2.4 Statistical analysis

All statistical analyses were conducted using R (version 4.3.1) and SPSS (version 26.0). The cohort was randomly allocated into a training set (n = 126) and a validation set (n = 54) at a 7:3 ratio. Continuous variables were expressed as median (interquartile range) and group comparisons using the t test or Mann-Whitney U-test. Categorical variables were expressed as n (%) and compared between groups using the chi-square test or Fisher's exact test. Univariate and multivariate logistic regression identified independent predictors to develop a clinical-ultrasound nomogram for individualized risk prediction. Furthermore, a dynamic nomogram was constructed using the "DynNom" and "shiny" packages in R. The area under the curve (AUC) values of the receiver operating characteristic (ROC) curves and a decision curve analysis (DCA) were used to evaluate the predictive performance and clinical utility of the model. Statistical tests were two-tailed and significance was set at $P < 0.05$.

3. Result

3.1 Participant characteristics

Table 1 summarizes the baseline clinical and ultrasonographic characteristics of the training and validation cohorts, with no statistically significant differences observed ($P > 0.05$). Detailed clinical and ultrasonographic characteristics and ultrasonographic features of SO patients and lesions are provided in Tables 2 and 3, respectively. Among SO cases, 65 patients (70.7%) were asymptomatic and incidentally detected during physical examinations or imaging studies. Notably, 3 patients (3.3%) were diagnosed during pregnancy. Laboratory findings revealed elevated CA125 levels (> 35 U/mL) in 23 patients (25.0%) and thyroid dysfunction in 12 patients (13.0%). Ascites was present in 7 patients (7.6%), fluid outside the pouch of Douglas. All assessed lesions were cystic-solid masses. 13 lesions (14.0%) were classified as O-RADS 4, and 80 lesions (86.0%) as O-RADS 5. In the initial ultrasonographic reports, 25 lesions (26.9%) were misclassified as malignant, and 37 lesions (39.8%) could not be definitively characterized. Postoperative pathological analysis revealed 69 cases (75.0%) of pure SO, 20 cases (21.7%) of SO combined with dermoid cyst, and 3 cases (3.3%) of SO combined with cystadenoma. Among these, 4 cases (4.3%) were malignant SO, 2 cases (2.2%) were carcinoid tumors, and 2 cases (2.2%) were microfocal papillary carcinoma, with no distant or local metastasis observed in any case. Regarding surgical management, 52 of 92 SO patients (56.5%) were premenopausal. Among these premenopausal patients, 9 (17.3%) underwent hysterectomy with bilateral salpingo-oophorectomy (BSO), including 3 who underwent open hysterectomy with BSO, which suggested potential overtreatment in some cases.

Table 1
Baseline characteristics in the training and test cohorts

Characteristics	Training (N = 126)	Testing (N = 54)	P
Age	52.00 (44.00–62.00)	51.50 (44.00-59.75)	0.713
Largest_diameter	7.10 (5.70–10.00)	6.75 (5.62–9.95)	0.670
Family_history			
No	109 (86.5%)	44 (81.5%)	0.524
Yes	17 (13.5%)	10 (18.5%)	
Symptom			
No	82 (65.1%)	33 (61.1%)	0.735
Yes	44 (34.9%)	21 (38.9%)	
O-RADS US			
4	17 (13.5%)	6 (11.1%)	0.846
5	109 (86.5%)	48 (88.9%)	
Ultrasound_assessment			
Benign	25 (19.8%)	7 (13.0%)	0.542
Malignant	45 (35.7%)	21 (38.9%)	
Uncertain	56 (44.4%)	26 (48.1%)	
Laterality			
Unilateral	112 (88.9%)	50 (92.6%)	0.626
Bilateral	14 (11.1%)	4 (7.4%)	

Data are given as n (%) or median (interquartile range). ORADS, the Ovarian-Adnexal Reporting and Data System.

Table 2
Clinical characteristics of women with SO (N = 92).

Variable	Value
Age	49.50(38.50, 61.00)
Menopausal	
No	52 (56.5%)
Yes	40 (43.5%)
Pregnant	
No	89 (96.7%)
Yes	3 (3.3%)
Abdominal_pain	
No	77 (83.7%)
Yes	15 (16.3%)
Abdominal_distension	
No	74 (80.4%)
Yes	18 (19.6%)
Irregular_bleeding	
No	86 (93.5%)
Yes	6 (6.5%)
Abdominal_mass	
No	89 (96.7%)
Yes	3 (3.3%)
Ascites	
No	85(92.4%)
Yes	7(7.6%)
Pregnant	
No	89 (96.7%)
Yes	3 (3.3%)
CA125	
≤ 35 U/mL	69 (75.0%)

Variable	Value
> 35 U/mL	23 (25.0%)
Thyroid_dysfunction	
No	80 (87.0%)
Yes	12 (13.0%)
Concomitant_disease	
No	69 (75.0%)
Dermoid cyst	20 (21.7%)
Cystadenoma	3 (3.3%)
Surgical_approach	
Laparoscopic conservative surgery	45 (48.9%)
Laparoscopic hysterectomy with BSO	27 (29.3%)
Open hysterectomy with BSO	19 (21.8%)

Data are given as n (%) or median (interquartile range). Clinical and laboratory variables were collected at the time of SO diagnosis. BSO: bilateral salpingo-oophorectomy.

Table 3
Ultrasonic features of the SO lesions (N = 93).

Variable	Value
Largest_diameter	6.40(4.90, 9.00)
O-RADS US	
4	13 (14.0%)
5	80 (86.0%)
Subjective ultrasound assessment	
Benign	31 (33.3%)
Malignant	25 (26.9%)
Uncertain	37 (39.8%)

Data are given as n (%) or median (interquartile range).

3.2 Clinical and ultrasound predictors for two diseases

Table 4 presents a comparative clinical indicators and ultrasound parameters of SO and early-stage HGSC in the training set. There were significant differences between the two groups for several variables, including CA125 ($p = 0.001$), heterogeneity of cyst fluid ($p = 0.025$), comet_tail artifact ($p = 0.036$), morphological pattern of the solid component ($p = 0.03$), and echogenicity of solid components ($p = 0.01$).

Table 4
Univariate and multivariate analyses of clinical and ultrasound indicators of SO and HGSC in training set.

Parameter	Univariate analysis			Multivariate analysis		
	HGSC	SO	P	OR	95%CI	P
Age	54.3 ± 8.9	48.3 ± 13.7	0.006	0.93	0.85–1.01	0.096
Family_history			0.053			
No	48 (77.4%)	57 (90.5%)				
Yes	14 (22.6%)	6 (9.5%)				
Symptom			0.087			
No	33 (53.2%)	43 (68.3%)				
Yes	29 (46.8%)	20 (31.7%)				
CA125			< 0.001	0.03	0.01–0.26	0.001
≤ 35 U/mL	10 (16.1%)	50 (79.4%)				
> 35 U/mL	52 (83.9%)	13 (20.6%)				
Largest_diameter	8.4 ± 3.8	7.3 ± 3.2	0.096			
Laterality			0.011	0.01	0.01-1308036.50	0.622
Unilateral	50 (80.6%)	62 (98.4%)				
Bilateral	12 (19.4%)	1 (1.6%)				
Vascularity			0.838			
No/Minimal	5 (8.1%)	7 (11.1%)				
Moderate	17 (27.4%)	16 (25.4%)				
Abundant	40 (64.5%)	40 (63.5%)				
Contour			0.172			

Parameter	Univariate analysis			Multivariate analysis		
	HGSC	SO	P	OR	95%CI	P
regular	36 (58.1%)	44 (69.8%)				
irregular	26 (41.9%)	19 (30.2%)				
Locular number			0.105			
≥ 5	24 (38.7%)	33 (52.4%)	0.010			
2–4	30 (48.4%)	28 (44.4%)	0.047			
1	8 (12.9%)	2 (3.2%)	0.036			
Cystic regularity			< 0.001			0.505
No	34 (59.6%)	20 (29%)				
Yes	23 (40.4%)	49 (71%)				
Cystic echogenicity			0.004	0.08	0.01–0.73	0.025
heterogeneous	20 (35.1%)	42 (60.9%)				
homogeneous	37 (64.9%)	27 (39.1%)				
Comet-tail artifact			< 0.001	7.01	1.13–43.54	0.036
No	55 (88.7%)	32 (50.8%)				
Yes	7 (11.3%)	31 (49.2%)				
Solid pattern			< 0.010			0.030
Intracystic solid component	28 (45.2%)	19 (30.2%)		Ref		
Extracystic solid component	8 (12.9%)	36 (57.1%)		13.49	1.53-118.52	0.019
Predominantly solid mass	26 (41.9%)	8 (12.7%)		0.94	0.14–6.27	0.953

Parameter	Univariate analysis			Multivariate analysis		
	HGSC	SO	P	OR	95%CI	P
Solid echogenicity			< 0.010			0.010
Hypoechoic	2 (3.2%)	40 (63.5%)		Ref		
Isoechoic	31 (50.0%)	20 (31.7%)		0.03	0.01–0.15	< 0.001
Hyperechoic	29 (46.8%)	3 (4.8%)		0.01	0.01–0.03	< 0.001
Calcification			0.654			
No	53 (85.5%)	52 (82.5%)				
Yes	9 (14.5%)	11 (17.5%)				
Free intraperitoneal fluid			0.239			
No	36 (58.1%)	43 (68.3%)				
Yes	26 (41.9%)	20 (31.7%)				

Data are given as n (%) or median (interquartile range). CI, confidence interval; OR, odds ratio.

Table 5
Diagnostic performance for differentiating SO from early-stage HGSC.

	AUC (95% CI)	ACC (95% CI)	SEN (95% CI)	SPE (95% CI)	PPV (95% CI)	NPV (95% CI)
Training Cohort	**0.971 (0.949–0.994)**	**0.92 (0.919–0.921)**	**0.952 (0.900-1.000)**	**0.887 (0.808–0.966)**	**0.896 (0.822–0.969)**	**0.948 (0.891-1.000)**
Testing Cohort	0.939 (0.882–0.995)	0.873 (0.869–0.877)	0.800 (0.657–0.943)	0.960 (0.883-1.000)	0.960 (0.883-1.000)	0.800 (0.657–0.943)

ACC, accuracy; **AUC**, area under the Curve; **ACC**, accuracy; **SEN**, sensitivity; **SPE**, specificity; **NPV**, negative predictive value; **PPV**, positive predictive value.

3.3 Model performance and validation

Using independent predictors derived from multivariable regression, a combined clinical-ultrasound nomogram was established to predict the probability of SO and early-stage HGSC (Fig. 1a). As shown in Table 5, the AUC was 0.971 (95%CI, 0.949–0.994) in the training cohort and 0.939 (95%CI, 0.882–0.995) in the testing cohort, with corresponding accuracy values of 0.920 (95%CI, 0.919–0.921) and 0.873 (95%CI, 0.869–0.877), respectively, indicating excellent discriminative ability between two diseases (Fig. 1b). Calibration curves demonstrated great agreement between predicted and observed probabilities in both cohorts, confirming satisfactory calibration (Fig. 1c). DCA showed favorable net clinical benefit across a wide range of threshold probabilities, validating its clinical utility for differentiating SO from early-stage HGSC (Fig. 1d, e).

Table 5 **Diagnostic performance for differentiating SO from early-stage HGSC.**

	AUC (95% CI)	ACC (95% CI)	SEN (95% CI)	SPE (95% CI)	PPV (95% CI)	NPV (95% CI)
Training Cohort	**0.971 (0.949–0.994)**	**0.92 (0.919–0.921)**	**0.952 (0.900-1.000)**	**0.887 (0.808–0.966)**	**0.896 (0.822–0.969)**	**0.948 (0.891-1.000)**
Testing Cohort	0.939 (0.882–0.995)	0.873 (0.869–0.877)	0.800 (0.657–0.943)	0.960 (0.883-1.000)	0.960 (0.883-1.000)	0.800 (0.657–0.943)

ACC, accuracy; **AUC**, area under the Curve; **ACC**, accuracy; **SEN**, sensitivity; **SPE**, specificity; **NPV**, negative predictive value; **PPV**, positive predictive value.

3.4 Utilization of individual prediction nomogram

To illustrate the clinical application workflow of the individualized risk prediction nomogram, this study enrolled four newly diagnosed cases of SO and early-stage HGSC respectively. We extracted their clinical and ultrasound variables and summed the scores corresponding to each predictive variable in the nomogram. Finally, the probability of SO and early-stage HGSC for each patient was calculated. The pathological diagnosis of SO in cases with higher predicted probabilities supports the accuracy of the model. This nomogram allows for an intuitive, quantifiable risk assessment and serves as a reference for preoperative risk stratification and clinical decision-making (Fig. 2).

3.5 Dynamic nomogram for Predicting SO

Building on the traditional risk prediction nomogram for distinguishing SO from early-stage HGSC, we created a dynamic online nomogram to enable more efficient and convenient individualized risk assessment. The website is: https://sopredict.shinyapps.io/Ovarian_Nomogram_App/(Figure S1).

3.6 The pathological basis of the morphological pattern of the solid component

The morphological pattern of the solid component differs significantly between SO and HGSC. In SO, the solid component is located along the cystic cavities. Although some larger cystic cavities may cause the intervening solid tissue to appear to protrude into the cavity, which can be mistakenly identified as papillary projections, three-dimensional (3D) ultrasound can more intuitively clarify their spatial relationship and highlight the hyperechoic features of the solid components (Fig. 3a-d). Careful observation usually reveals a continuous and smooth cyst wall between the solid components and the cyst cavity, which contrasts with the genuine papillary projections or mural nodules in HGSC, where the intracystic excrescences disrupt the smooth inner wall (Fig. 3e-h). In addition, MRI also supported this observation. The signal within SO cystic cavities can present a "stained glass appearance" due to variations in colloid viscosity and concentration, and cyst wall or septa may show enhancement, but no obvious enhancement of solid components within the cystic cavities has been described [18, 23].

Pathologically, these imaging differences reflect distinct tissue origins. SO presents as a solid mass with scattered round or oval cystic cavities lined by smooth walls and filled with abundant colloid-like material. The solid components of SO correspond to thyroid tissue consisting of follicular epithelium and vascular-rich fibrous stroma. These cystic cavities tend to originate from thyroid follicles or cystic degeneration, lack solid components [4, 24, 25]. In contrast, HGSC commonly appears as grayish-yellow solid mass with hemorrhage, necrosis, and irregular cystic cavities (Fig. 4). It is characterized by high-grade malignant epithelial proliferation with fibrovascular cores, and papillae and mural nodules may project into cystic spaces and show invasive growth [26–28].

3.7 Characteristic ultrasonic signs of SO

To enhance model interpretability, we summarized three characteristic ultrasound signs of SO, all of which align with the ultrasound variables selected by the model. They share the following common characteristics: the isoechoic to hyperechoic solid components are distributed peripherally or between cystic cavities without intracystic protrusion, forming stable peripheral scaffold-like or ring-liked structures. The cyst contents are heterogeneous and occasional show comet-tail artifact. The three specific ultrasonographic features include: (1) *Ovary-like sign*: Multiple round or oval cystic locules within the solid component form an ovary-like appearance; (2) *palette sign*: a well-defined solid core surrounded by multiple cysts containing heterogeneous contents, creating a petal configuration; (3) *Cheerios sign*: A well-circumscribed, hyperechoic solid area with a central cyst within a multilocular-solid mass. (Fig. 5).

3.8 Reinterpretation of the Pearl Sign

Previous studies have suggested that the "pearl sign" is a specific ultrasonographic feature of SO, corresponding to the "petal sign" proposed above. It is described as a smooth roundish solid area with vascularization [13, 14, 29]. In our cases, the hyperechoic solid components in SO are typically peripheral to cystic cavities with moderate to intense vascularity, as they derive from thyroid tissue (Fig. 6a,b). Notably, the "pseudopearl sign" from deposits arises from the gradual deposition and compaction of intracystic colloid over time, appearing as hypoechoic or hyperechoic flocculent aggregates and may be

misinterpreted as the "pearl sign"(Fig. 6e-h) [27, 30]. Unlike true thyroid tissue, these colloid deposits may show slight deformation or displacement with postural changes or pressure from the operator and generally show no internal blood flow signals on color Doppler ultrasound(Fig. 6c,d). The IOTA group categorized such deposits as a pitfall in distinguishing intracystic solid components and recommended, Doppler and dynamic scanning to reduce errors [31]. Distinguishing these signs is critical to minimize misdiagnosis and validate the "pearl sign" specificity for SO. Only excluding colloid deposition can reliably assess its true value.

4. Discussion

Currently, cystic-solid SO lesions are frequently classified as O-RADS US 4/5, which fails to support precise risk stratification from malignant ovarian tumors. Due to the rarity of SO, relevant studies are mostly limited to case reports or small retrospective series, lacking evidence-based differentiation models. In this study, we specifically focused on O-RADS US 4/5 SO and used the most prevalent ovarian malignancy as a comparator to develop and validate a static and dynamic individualized prediction model. This model showed excellent discrimination and clinical utility for preoperative risk stratification, providing a methodological reference for future research on differentiating SO from other ovarian tumor types. Importantly, we discovered three specific ultrasound signs of SO that are consistent with independent ultrasound predictors in the model. Furthermore, by elucidating the morphological pattern of the solid component and the " pearl sign" in SO, we have enhanced the statistical credibility and clinical usability of the model.

The predictors in our model are grounded in definitive clinicopathological evidence and reflect the distinct histological features of SO and the aggressive biological behavior of HGSC. The key predictor is the extracystic location and hyperechoic appearance of the solid component. Pathologically, the solid component of SO corresponds to thyroid tissue, composed of densely packed thyroid follicles and fibrous stroma. The cystic areas on ultrasonography often correspond to colloid-filled dilated follicles or cystic degeneration. Therefore, the solid components typically distribute along the periphery of locules and present as ring-like or septal-like focal thickening. Given that abundant follicular interfaces act as acoustic scatterers, the solid component typically appears iso- to hyperechoic on ultrasonography [4, 25, 29]. In contrast, HGSC is characterized by invasive proliferation of highly atypical malignant epithelial cells, often forming papillary projections or irregular nodules. It is also prone to necrosis and hemorrhage, leading to heterogeneous hypoechoic or mixed echogenicity appearances [27, 28, 32]. Secondly, heterogeneous cyst fluid and comet-tail artifacts directly reflect colloid-rich locules in SO [39]. The locules of SO are essentially thyroid follicles filled with colloid of varying concentrations. Variation in colloid concentration causes heterogeneous intralocular echogenicity. When colloid becomes highly concentrated and develops granular or crystalline contents, punctate echogenic foci may be observed. The acoustic interface between liquid colloid and condensed particulate material can generate comet-tail artifact [29, 33, 34]. Although HGSC may also show heterogeneous cystic echogenicity due to hemorrhage or necrosis, these findings are generally nonspecific and typically lack these specific colloid-

related features. CA125, a broad biomarker for ovarian cancer, is more frequently elevated in HGSC, but may remain normal in early-stage cases [35]. Nevertheless, CA125 may also be elevated in SO complicated by pseudo-Meigs syndrome with ascites [36, 37].

The three characteristic ultrasonic signs of SO identified in this study—ovary-like sign, palette sign, and cheerios sign—collectively form a specific morphologic signature. They consistently show a peripheral, iso- to hyperechoic solid component surrounding the locules, forming a stable scaffold-like or encircling architecture, with multiple cystic spaces exhibiting heterogeneous internal echogenicity. These patterns offer radiologists intuitive and reproducible diagnostic criteria that align with the histologic basis of SO and may improve diagnostic consistency and accuracy.

The clinical significance is reflected in three aspects. Firstly, the dynamic nomogram enhances the operability of the abstract statistical model by providing an intuitive graphical tool. This advancement improves preoperative diagnostic efficiency and facilitates future clinical promotion and multicenter validation. Secondly, the consistency between the three characteristic ultrasound signs and the independent predictors from multivariate analysis validates the credibility of the diagnostic evidence. Thirdly, by reinterpreting the spatial architecture and the “pearl sign” based on the pathophysiology, this study clarified the morphological pattern of SO and distinguished the “pearl sign” derived from thyroid tissue from the “pseudopearl sign” caused by intracystic colloid deposition, providing crucial evidence for reducing misdiagnosis.

The model offers unambiguous guidance for clinical management. For patients suspected of SO, particularly those with fertility desires or during pregnancy, this can reinforce confidence in follow-up observation and avoid unnecessary laparotomy. Thus, this tool facilitates customized surgical strategies and provides a framework for precise preoperative risk stratification and management. Nevertheless, several limitations should be acknowledged. Double reading and expert confirmation improved the consistency, but retrospective design may not eliminate subjective bias. Single-center dataset without external validation also limited generalizability. Future multicenter prospective studies are needed to further verify robustness and facilitate broader clinical adoption. Moreover, the model currently distinguishes only SO from HGSC, subsequent studies must include other malignant epithelial malignancy to enhance clinical utility.

5. Conclusions

We developed and validated the first static and dynamic nomogram for differentiate O-RADS US 4/-5 SO from early-stage HGSC, providing a visualized decision support tool for a major preoperative diagnostic challenge. From a pathophysiological perspective, we elucidated the key morphological patterns of SO, systematically summarized three SO-specific ultrasonographic signs, and reinterpreted the “pearl sign”. In short, these findings may support more accurate, strategic preoperative decision-making.

Abbreviations

SO
Struma ovarii
US
Ultrasound
O-RADS
Ovarian-Adnexal Reporting and Data System
MRI
Magnetic resonance imaging
HGSC
High-grade serous ovarian carcinoma
FIGO
International Federation of Gynecology and Obstetrics
ROC
Receiver operating characteristic
AUC
Area under the curve
DCA
Decision curve analysis
CI
Confidence interval
BSO
Bilateral salpingo-oophorectomy
IOTA
International Ovarian Tumor Analysis

Declarations

Ethics approval and consent to participate

This retrospective study followed the Declaration of Helsinki and was approved by both the Institutional Ethics Committee (approval No. JS-3232) and the Institutional Review Board (approval No. I-24PJ0809) of Peking Union Medical College Hospital. All methods were performed in accordance with relevant guidelines and regulations. The requirement for written informed consent was waived due to the retrospective nature of the study.

Consent for publication

Consent for publication was obtained from all individual participants whose data are included in this study.

Availability of data and material

The datasets used and/or analysed during the current study are available from thecorresponding author on reasonable request.

Competing interests

The authors declare that they have no competing interests.

Funding

This work was supported by the National Key R&D Program of China (2023YFC2411705), the National Natural Science Foundation of China (U22A2023, 62325112, and 82402293), the PUMCH Talent Development Support Program (ULJ04684), and the National High-Level Hospital Clinical Research Funding (2022-PUMCH-D-002).

Authors' contributions

All authors contributed significantly to this work. Wanting Chen and Fei Ji contributed equally to this work and share first authorship. They were involved in study conception, data collection, data analysis, and manuscript drafting. Weihan Xiao and Jiajia Jiajia participated in data collection, data sorting, and result interpretation. Wenjing Zhao was responsible for scientific illustration and chart drawing. Jinghui Liang contributed to data collection and literature collection. Na Su and Meng Yang are the corresponding authors, responsible for study design, supervision, critical revision of the manuscript, and final approval of the version to be published. All authors read and approved the final manuscript.

Acknowledgements

Not applicable

References

1. Willemse PH, Oosterhuis JW, Aalders JG, et al. Malignant struma ovarii treated by ovariectomy, thyroidectomy, and 131I administration. Cancer. 1987;60(2):178–82. https://doi.org/10.1002/1097-0142(19870715)60:2%3C178::aid-cncr2820600210%3E3.0.co;2-q.
2. Makani S, Kim W, Gaba AR. Struma Ovarii with a focus of papillary thyroid cancer: a case report and review of the literature. Gynecol Oncol. 2004;94(3):835–9. https://doi.org/10.1016/j.ygyno.2004.06.003.
3. Fujiwara S, Tsuyoshi H, Nishimura T, Takahashi N, Yoshida Y. Precise preoperative diagnosis of struma ovarii with pseudo-Meigs' syndrome mimicking ovarian cancer with the combination of (131)I scintigraphy and (18)F-FDG PET: case report and review of the literature. J Ovarian Res. 2018;11(1):11. https://doi.org/10.1186/s13048-018-0383-2.
4. Tondi Resta I, Sande CM, LiVolsi VA. Neoplasms in Struma Ovarii: A Review. Endocr Pathol. 2023;34(4):455–60. https://doi.org/10.1007/s12022-023-09789-7.

5. Yoo SC, Chang KH, Lyu MO, Chang SJ, Ryu HS, Kim HS. Clinical characteristics of struma ovarii. J Gynecol Oncol. 2008;19(2):135–8. https://doi.org/10.3802/jgo.2008.19.2.135.
6. Egan C, Stefanova D, Thiesmeyer JW, et al. Proposed Risk Stratification and Patterns of Radioactive Iodine Therapy in Malignant Struma Ovarii. Thyroid. 2022;32(9):1101–8. https://doi.org/10.1089/thy.2022.0145.
7. Goffredo P, Sawka AM, Pura J, Adam MA, Roman SA, Sosa JA. Malignant struma ovarii: a population-level analysis of a large series of 68 patients. Thyroid. 2015;25(2):211–5. https://doi.org/10.1089/thy.2014.0328.
8. Gobitti C, Sindoni A, Bampo C, et al. Malignant struma ovarii harboring a unique NRAS mutation: case report and review of the literature. Horm (Athens). 2017;16(3):322–7. https://doi.org/10.14310/horm.2002.1750.
9. Kempers RD, Dockerty MB, Hoffman DL, Bartholomew LG. Struma ovarii–ascitic, hyperthyroid, and asymptomatic syndromes. Ann Intern Med. 1970;72(6):883–93. https://doi.org/10.7326/0003-4819-72-6-883.
10. Li S, Yang T, Xiang Y, Li X, Zhang L, Deng S. Clinical characteristics and survival outcomes of malignant struma ovarii confined to the ovary. BMC Cancer. 2021;21(1):383. https://doi.org/10.1186/s12885-021-08118-7.
11. Tamura N, Murakami K, Ozaki R, et al. Current state of management of struma ovarii and preoperative imaging features: A retrospective case series study of 18 patients at a single institution. J Obstet Gynaecol Res. 2023;49(3):1007–11. https://doi.org/10.1111/jog.15545.
12. Strachowski LM, Jha P, Phillips CH, et al. Radiology. 2023;308(3):e230685. https://doi.org/10.1148/radiol.230685. O-RADS US v2022: An Update from the American College of Radiology's Ovarian-Adnexal Reporting and Data System US Committee.
13. Savelli L, Testa AC, Timmerman D, Paladini D, Ljungberg O, Valentin L. Imaging of gynecological disease (4): clinical and ultrasound characteristics of struma ovarii. Ultrasound Obstet Gynecol. 2008;32(2):210–9. https://doi.org/10.1002/uog.5396.
14. Weinberger V, Kadlecova J, Minář L, et al. Struma ovarii - ultrasound features of a rare tumor mimicking ovarian cancer. Med Ultrason. 2018;20(3):355–61. https://doi.org/10.11152/mu-1526.
15. Chen M, Liao S, Xu Y, Ye X, Jia X, Zhang S. Clinicopathological and imaging features of struma ovarii: a retrospective study. Front Oncol. 2025;15:1487812. https://doi.org/10.3389/fonc.2025.1487812.
16. Matsuki M, Kaji Y, Matsuo M, Kobashi Y. Struma ovarii: MRI findings. Br J Radiol. 2000;73(865):87–90. https://doi.org/10.1259/bjr.73.865.10721328.
17. Ye R, Zheng Y, Pan F, Wang H, Yan C, Li Y. Differentiating struma ovarii from FIGO stage I malignant ovarian tumors in O-RADS MRI 5 lesions: a targeted cohort study. Abdom Radiol (NY). 2025;50(3):1426–34. https://doi.org/10.1007/s00261-024-04564-6.
18. Ishiguro T, Saida T, Shikama A, et al. Diagnostic imaging analysis to differentiate struma ovarii from mucinous carcinomas, encompassing T2*-based imaging, diffusion-weighted imaging, and dynamic

contrast-enhanced imaging. Br J Radiol. 2024;97(1163):1843–9. https://doi.org/10.1093/bjr/tqae165.

19. Caruso G, Weroha SJ, Cliby W. Ovarian Cancer: A Review. JAMA. 2025;334(14):1278–91. https://doi.org/10.1001/jama.2025.9495.
20. Eisenhauer EA. Real-world evidence in the treatment of ovarian cancer. Ann Oncol. 2017;28(suppl8):viii61–5. https://doi.org/10.1093/annonc/mdx443.
21. Kraemer B, Grischke EM, Staebler A, Hirides P, Rothmund R. Laparoscopic excision of malignant struma ovarii and 1 year follow-up without further treatment. Fertil Steril. 2011;95(6):2124. https://doi.org/10.1016/j.fertnstert.2010.12.047. .e9-12.
22. Llueca A, Maazouzi Y, Herraiz JL, et al. Treatment and follow-up in an asymptomatic malignant struma ovarii: A case report. Int J Surg Case Rep. 2017;40:113–5. https://doi.org/10.1016/j.ijscr.2017.09.005.
23. Hassan SA, Akhtar A, Falah NU, Sheikh FN. Malignant Thyroid-type Papillary Neoplasm in Struma Ovarii: A Case Report. Cureus. 2019;11(12):e6450. https://doi.org/10.7759/cureus.6450.
24. Wei S, Baloch ZW, LiVolsi VA. Pathology of Struma Ovarii: A Report of 96 Cases. Endocr Pathol. 2015;26(4):342–8. https://doi.org/10.1007/s12022-015-9396-1.
25. Fitzpatrick M, Olkhov-Mitsel E, Amemiya Y, et al. Clinicopathologic, Immunohistochemical, and Molecular Analysis of Primary Ovarian Carcinoid Tumors With Correlation of Ki67 Proliferation Index With Patient Outcomes. Mod Pathol. 2025;38(11):100822. https://doi.org/10.1016/j.modpat.2025.100822.
26. Taylor EC, Irshaid L, Mathur M. Multimodality Imaging Approach to Ovarian Neoplasms with Pathologic Correlation. Radiographics. 2021;41(1):289–315. https://doi.org/10.1148/rg.2021200086.
27. Hassen K, Ghossain MA, Rousset P, et al. Characterization of papillary projections in benign versus borderline and malignant ovarian masses on conventional and color Doppler ultrasound. AJR Am J Roentgenol. 2011;196(6):1444–9. https://doi.org/10.2214/ajr.10.5014.
28. Moro F, Baima Poma C, Zannoni GF, et al. Imaging in gynecological disease (12): clinical and ultrasound features of invasive and non-invasive malignant serous ovarian tumors. Ultrasound Obstet Gynecol. 2017;50(6):788–99. https://doi.org/10.1002/uog.17414.
29. Feng Y, Chen Y, Wu Q, Bao Z, Ning C, Zhao C. A retrospective case series at a tertiary hospital in china: ultrasonographic features of Struma ovarii. BMC Cancer. 2025;25(1):1180. https://doi.org/10.1186/s12885-025-14606-x.
30. Zannoni L, Savelli L, Jokubkiene L, et al. Intra- and interobserver agreement with regard to describing adnexal masses using International Ovarian Tumor Analysis terminology: reproducibility study involving seven observers. Ultrasound Obstet Gynecol. 2014;44(1):100–8. https://doi.org/10.1002/uog.13273.
31. Timmerman D, Valentin L, Bourne TH, Collins WP, Verrelst H, Vergote I. Terms, definitions and measurements to describe the sonographic features of adnexal tumors: a consensus opinion from

the International Ovarian Tumor Analysis (IOTA) Group. Ultrasound Obstet Gynecol. 2000;16(5):500–5. https://doi.org/10.1046/j.1469-0705.2000.00287.x.

32. Vang R, Shih Ie M, Kurman RJ. Ovarian low-grade and high-grade serous carcinoma: pathogenesis, clinicopathologic and molecular biologic features, and diagnostic problems. Adv Anat Pathol. 2009;16(5):267–82. https://doi.org/10.1097/PAP.0b013e3181b4fffa.
33. Malhi H, Beland MD, Cen SY, et al. Echogenic foci in thyroid nodules: significance of posterior acoustic artifacts. AJR Am J Roentgenol. 2014;203(6):1310–6. https://doi.org/10.2214/ajr.13.11934.
34. Wu H, Zhang B, Li J, Liu Q, Zhao T. Echogenic foci with comet-tail artifact in resected thyroid nodules: Not an absolute predictor of benign disease. PLoS ONE. 2018;13(1):e0191505. https://doi.org/10.1371/journal.pone.0191505.
35. Kaaks R, Cooley V, Mukama T, et al. A Prospective Study Consortium for the Discovery and Validation of Early Detection Markers for Ovarian Cancer - Baseline Findings for CA125. Clin Cancer Res. 2025;31(12):2441–53. https://doi.org/10.1158/1078-0432.Ccr-24-1845.
36. Li S, Hong R, Yin M, Zhang X, Zhang T, Yang J. Struma ovarii with synchronous ascites and elevated CA125 level: a retrospective cohort study. Acta Oncol. 2023;62(8):889–96. https://doi.org/10.1080/0284186x.2023.2226798.
37. Wang S, He X, Yang H, Chen L. Struma Ovarii Associated with Ascites and Elevated CA125: Two Case Reports and Review of the Literature. Int J Womens Health. 2022;14:1291–6. https://doi.org/10.2147/ijwh.S379128.

Figures

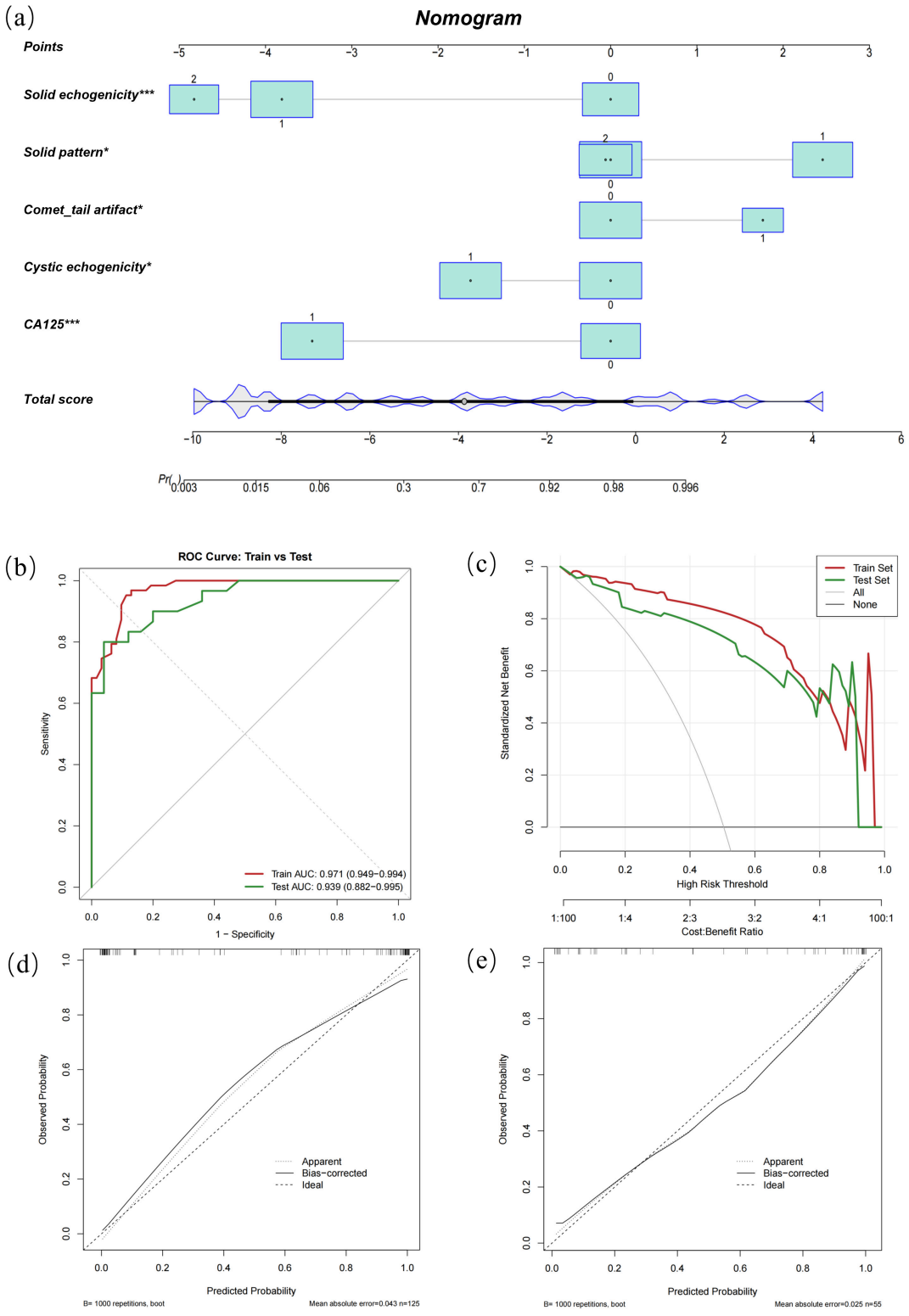


Figure 1

Nomogram for preoperative discrimination between struma ovarii (SO) and high-grade serous carcinoma (HGSC). The nomogram was constructed from multivariate logistic regression analysis (A). To determine the risk of SO, points are assigned for each variable according to the position along the 'points' scale, summed, and the corresponding probability is identified on the total points scale. Receiver operating

characteristic (ROC) curves (B), decision curve analysis (DCA) (C), and calibration curves in the training (D) and calibration curve in the test set (E).

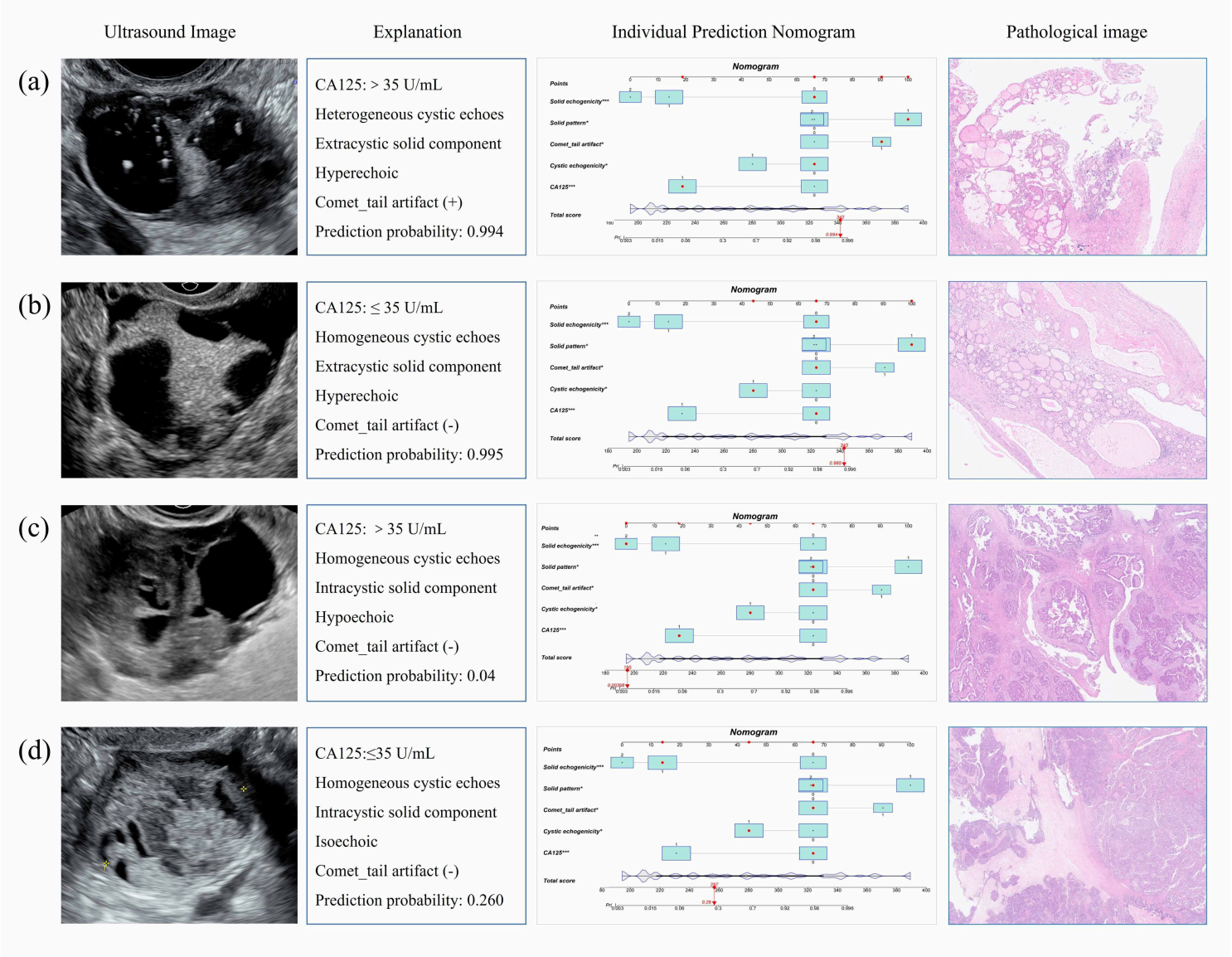


Figure 2

Representative application of the individualized prediction nomogram for SO (a,b) and HGSC (c,d). The probability of SO was calculated based on the five selected predictor variables.

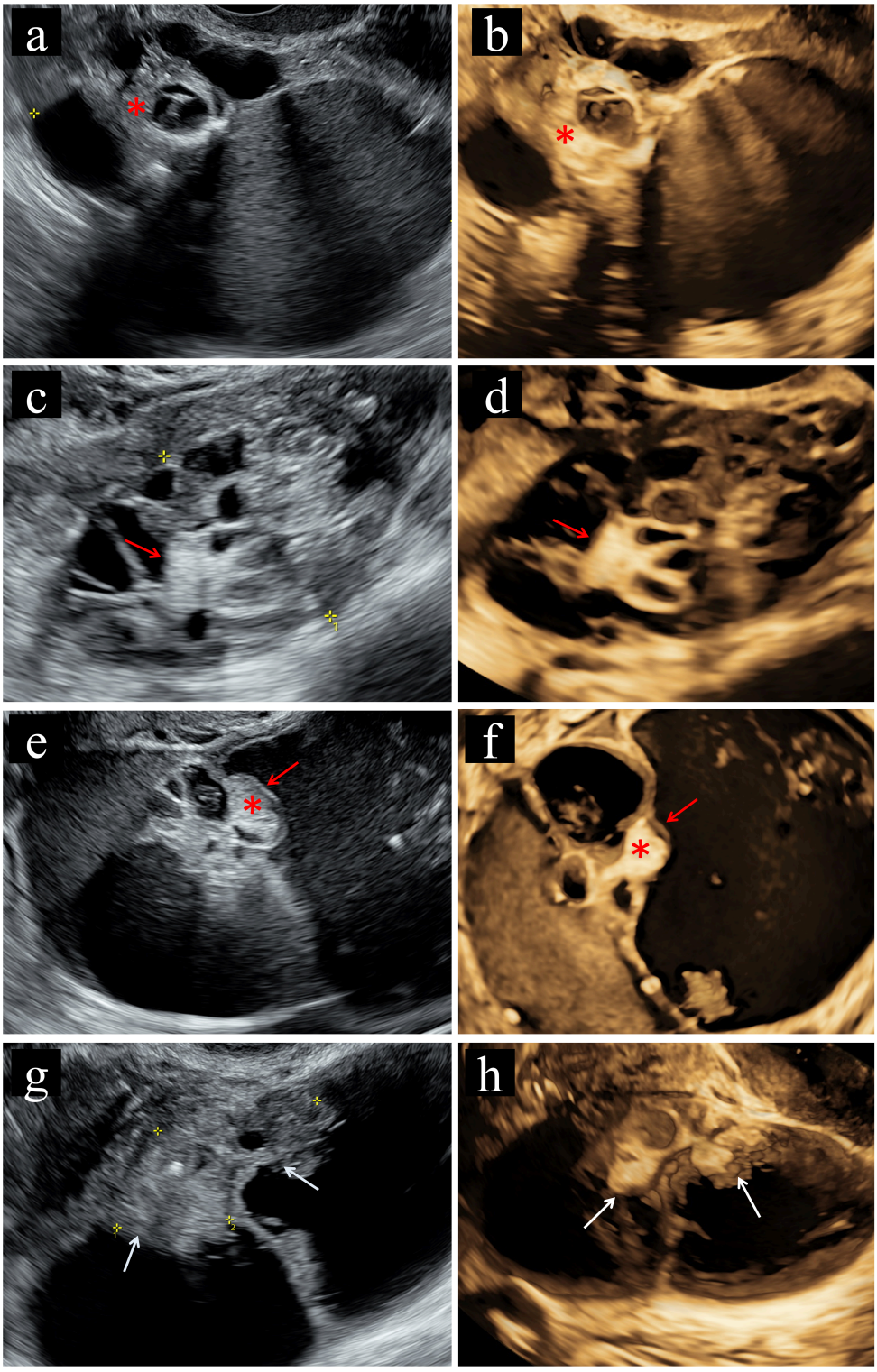


Figure 3

Grayscale ultrasound and three-dimensional (3D) rendering of SO and HGSC. 3D ultrasound more clearly demonstrates the solid components located at the periphery of locules, which present as ring-like (asterisks in a, b) or septal-like focal thickening (arrows in c, d) in SO. The arrow in (e,f) points to a continuous cyst wall in SO, and the asterisk marks the extracystic solid component. The arrows in (g,h) point to solid papillary projections in HGSC.

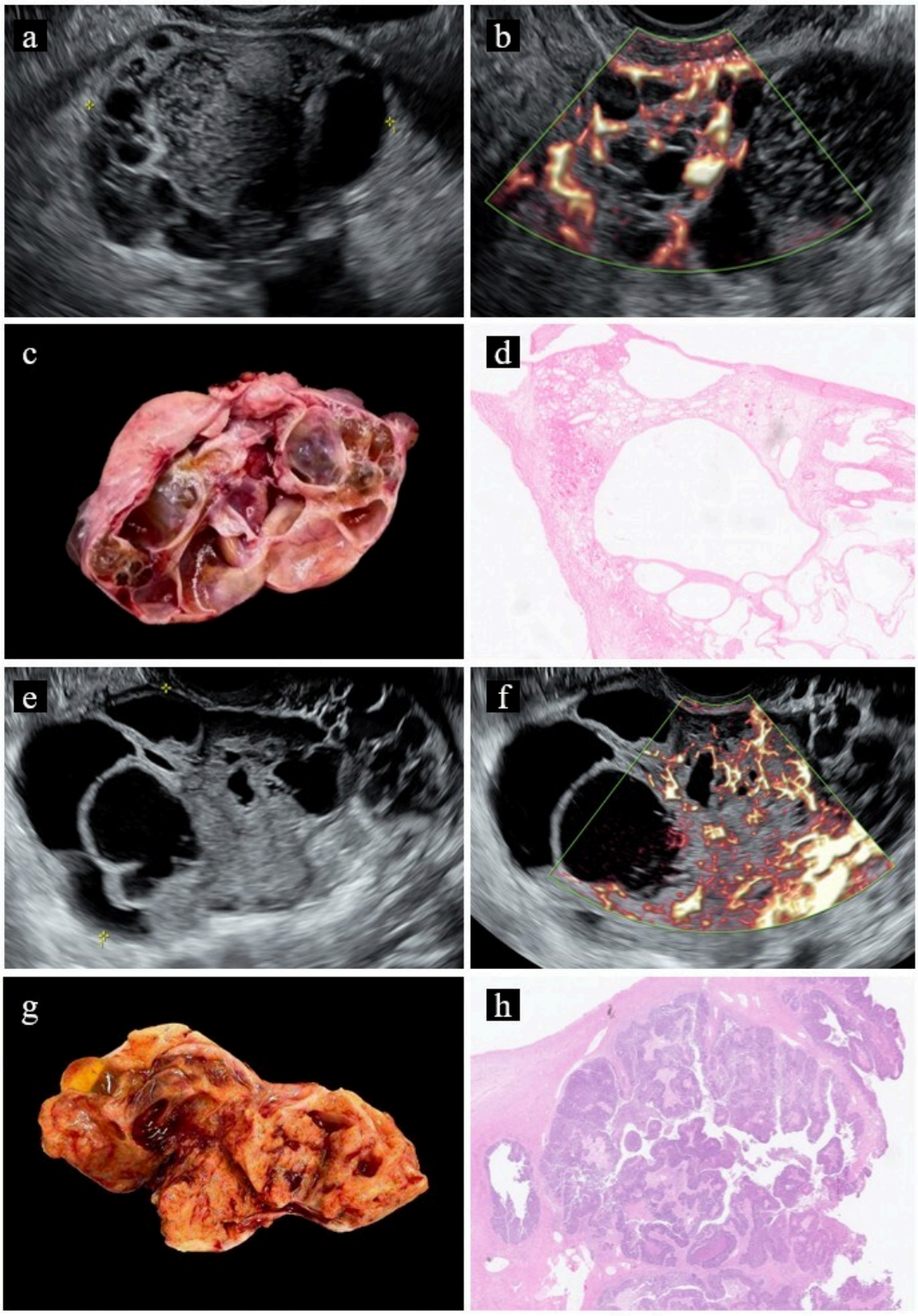


Figure 4

Grayscale ultrasound images (a, e), corresponding microvascular images (b, f), macroscopic appearance (c, g), and histopathology (d, f), and for SO (a-d) and HGSC (e-h).

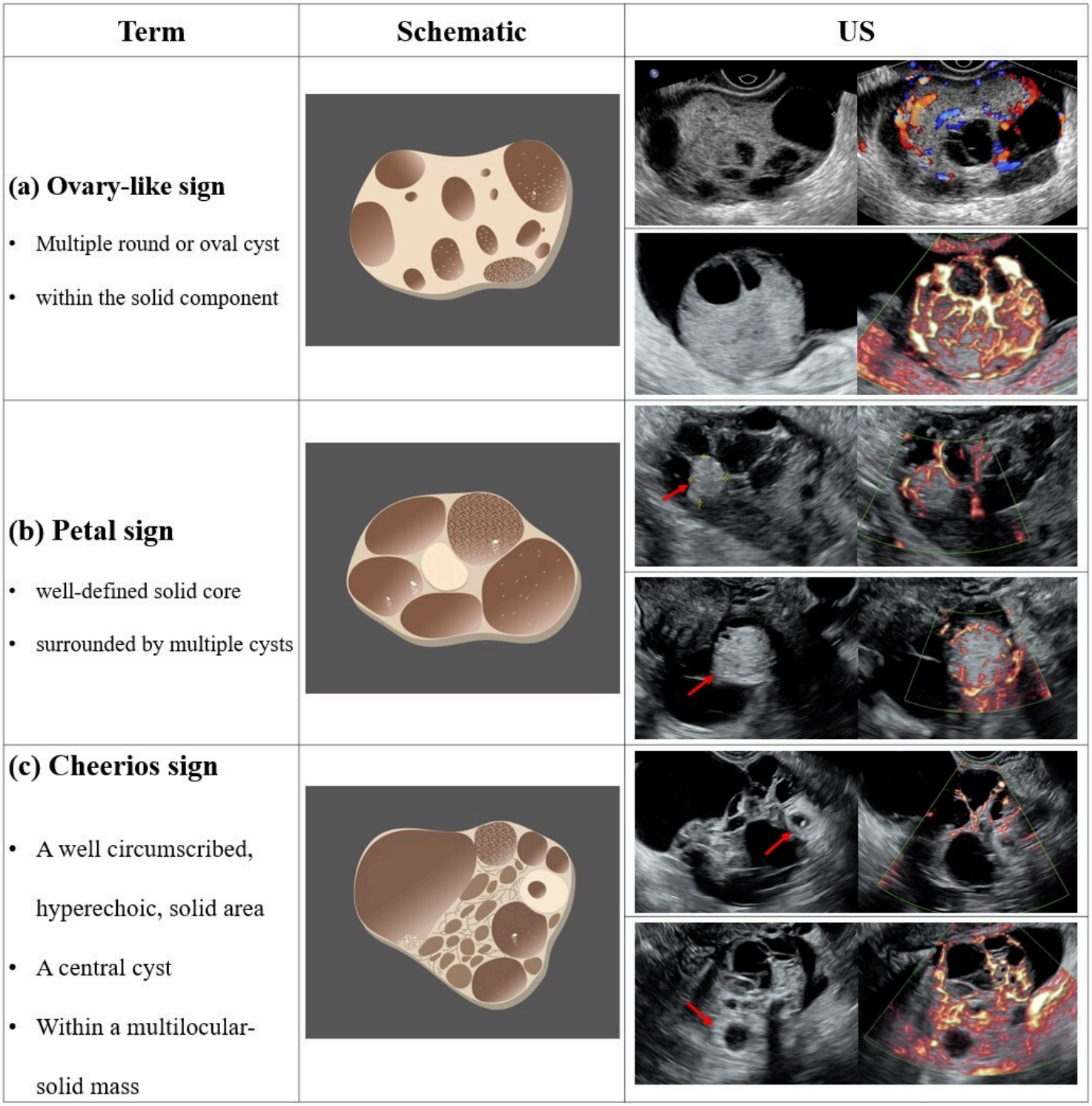


Figure 5

Typical ultrasound signs and schematic illustrations of SO. (a) Ovary-like sign. (b) palette sign. The arrows in (b) points to solid core. (c) Cheerios sign. The arrows in (c) points to hyperechoic ring.

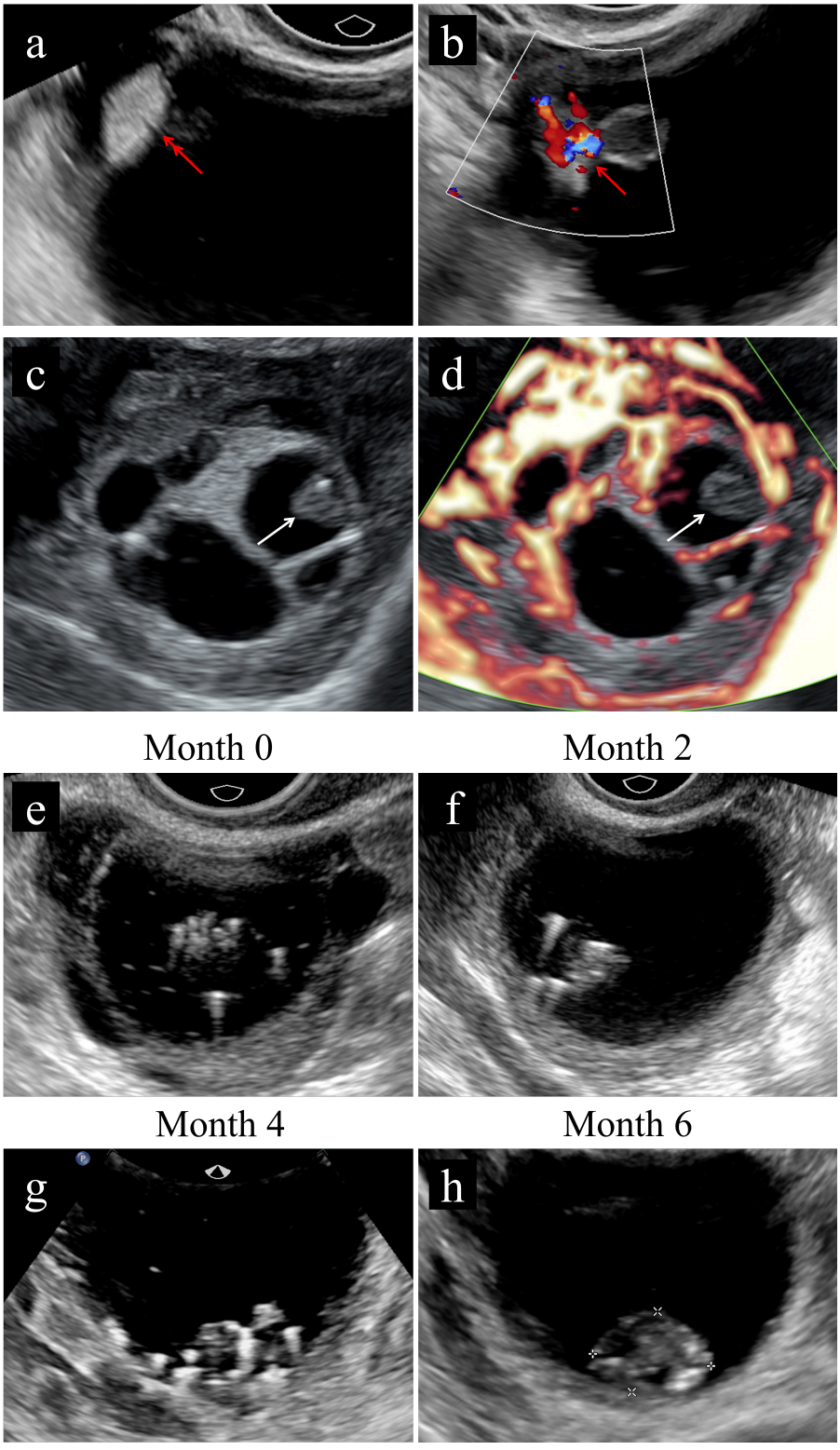


Figure 6

Pearl sign and pseudopearl sign in SO on ultrasound. Grayscale (a) and color Doppler (b) images illustrating the “pearl sign” (arrows) from thyroid tissue in Patient 1. Grayscale (c) and color Doppler (d) images illustrating the “pseudopearl sign” (arrows) from deposits in Patient 2. (e–h) Sequential development of the “pseudopearl sign” from colloid within a cystic cavity of SO. The images show the

dynamic formation process, including deposition (Months 0, 2), aggregation (Month 4), and compaction (Month 6).

Supplementary Files

This is a list of supplementary files associated with this preprint. Click to download.

- Supplement.doc